Nano-electrochemistry & Nano-photochemistry
https://www.sciltp.com/journals/nenp

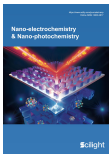

Article

A Flexible Copper-Doped Laser-Induced Graphene-Based Sensor for the Multiplexed Detection of Sweat Metabolites

Hongbin Chen, Haojun Zhang, Ming Gao, Nianyue Cao, Xingchao Liu, Xirui Chen, Panpan Gai * and Chengcheng Gu *

College of Chemistry and Pharmaceutical Sciences, Qingdao Agricultural University, Qingdao 266109, China
* Correspondence: ppgai@qau.edu.cn (P.G.); ccgu@qau.edu.cn (C.G.)

How To Cite: Chen, H.; Zhang, H.; Gao, M.; et al. A Flexible Copper-Doped Laser-Induced Graphene-Based Sensor for the Multiplexed Detection of Sweat Metabolites. *Nano-electrochemistry & Nano-photochemistry* **2026**, *2*(1), 1. https://doi.org/10.53941/nenp.2026.100001

Received: 8 December 2025
Revised: 23 December 2025
Accepted: 25 December 2025
Published: 19 January 2026

Abstract: Despite advances in wearable sweat sensors, the simultaneous detection of multiple analytes remains a challenge due to signal overlap. Ascorbic acid (AA), dopamine (DA), and uric acid (UA) are promising biomarkers for early diagnostics, but their similar oxidation potentials impede selective detection on conventional electrodes. To overcome this limitation, we developed a flexible sensor based on a copper-doped laser-induced graphene (Cu-LIG) electrode for the separate and simultaneous detection of these three biomarkers. The Cu-LIG electrode exhibits enhanced electrocatalytic activity compared to pristine LIG and performs effectively in artificial sweat. Cyclic voltammetry and differential pulse voltammetry confirm its improved electrochemical performance, including high sensitivity and low detection limits. This electrode demonstrates strong potential for integration into flexible, wearable health-monitoring devices.

Keywords: copper-doped LIG; electrochemical detection; sweat metabolites; multiplexed detection

1. Introduction

Individualized health monitoring and decentralized diagnostics are rapidly advancing, propelled by the growing demand for real-time, person-specific physiological data [1]. In this context, wearable electrochemical sensors for non-invasive sweat analysis have emerged as a transformative technology [2–5]. These devices enable continuous, on-body monitoring of a broad spectrum of chemical biomarkers, offering a patient-friendly alternative to blood-based measurements [6–10]. Sweat comprises a dynamic mixture of biomolecules that reflect systemic physiological states. Among these, ascorbic acid (AA), dopamine (DA), and uric acid (UA) represent a critical group of interrelated analytes [4,11–13]. These molecules play essential and often interconnected roles in regulating metabolism, neurological function, and redox homeostasis. Specifically, AA is a key antioxidant whose imbalance is associated with oxidative stress [14,15]; DA is a vital neurotransmitter, with abnormal levels linked to neurodegenerative disorders such as Parkinson's disease [16]; and elevated UA, a product of purine catabolism, serves as a biomarker for gout and renal dysfunction [17–20]. Therefore, the simultaneous and high-sensitivity monitoring of these three biomarkers with high temporal resolution is crucial for achieving a holistic, real-time assessment of an individual's health status.

Electrochemical sensing platforms are ideally suited for wearable applications due to their operational simplicity, low cost, rapid response, and high sensitivity [4]. However, the simultaneous detection of AA, DA, and UA is severely hampered by the significant overlap of their voltametric peaks at conventional electrodes, leading to severe signal interference that compromises selectivity in complex biofluids like sweat [21]. This fundamental limitation necessitates the rational engineering of advanced electrode materials to decouple these overlapping signals for high-performance wearable biosensors. Among various candidates, carbon-based architectures, particularly graphene, are popular due to their high electrical conductivity, large specific surface area, and excellent

chemical stability [4]. Laser-induced graphene (LIG) has recently emerged as a premier material for flexible sensing, enabling direct, single-step fabrication of three-dimensional porous graphene on flexible polymers, thus providing a scalable and cost-effective route to create conductive scaffolds for wearable devices [12,22]. Nonetheless, the sensing performance of pristine LIG is often constrained by limited selectivity and sensitivity. Incorporating heteroatom dopants or metal-based modifiers can effectively tune its electronic structure, increase the density of active sites, and substantially enhance electrocatalytic activity, enabling reliable operation in complex physiological environments [23]. In particular, transition metal nanomaterials such as copper nanoparticles (Cu NPs) are highly promising owing to their excellent electrocatalytic properties, conductivity, and low cost [24]. They are known to promote electron-transfer kinetics and lower reaction overpotentials, thereby improving overall sensor sensitivity and selectivity [25]. Therefore, the synergistic integration of Cu NPs with the 3D porous LIG framework presents a compelling strategy to form a high-performance composite sensing interface [26].

Herein, we develop a secondary laser printing method for the efficient and uniform integration of Cu NPs onto flexible LIG, resulting in a synergistic copper-doped (Cu-LIG) composite electrode (Scheme 1). This architecture leverages the high surface area of the 3D porous LIG scaffold and the superior electrocatalysis of Cu NPs, which collectively markedly enhance the overall electrochemical activity. The sensing performance for the simultaneous detection of AA, DA, and UA was evaluated using cyclic voltammetry (CV) and differential pulse voltammetry (DPV). The results confirm the excellent capability of the sensor for sensitive and well-resolved multiplexed detection of these three biomarkers in sweat. This fabrication strategy thus provides an effective pathway for developing non-invasive, wearable sensors toward personalized health management.

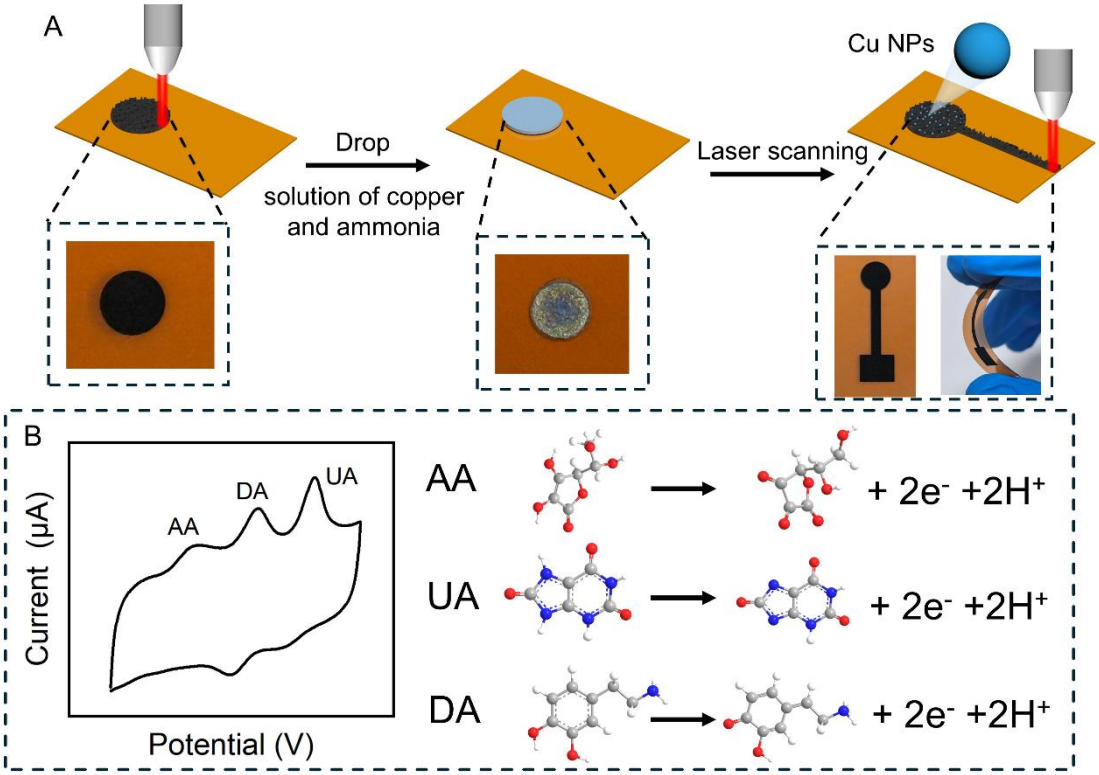

Scheme 1. Fabrication and application of the Cu-LIG sensor. (**A**) Schematic illustration of the two-step laser printing process for in-situ copper doping onto laser-induced graphene (LIG). (**B**) Diagram depicting the application of the flexible Cu-LIG electrode for the multiplexed electrochemical detection of AA, DA, and UA in sweat.

2. Materials and Methods

2.1. Chemicals and Reagents

All chemicals were of analytical grade and used without further purification. Uric acid ($C_5H_4N_4O_3$), ascorbic acid ($C_6H_8O_6$), dopamine ($C_8H_{11}NO_2$), glucose ($C_6H_{12}O_6$), ammonium chloride (NH_4Cl), urea (CH_4N_2O), lactic acid ($C_3H_6O_3$), potassium ferricyanide ($K_3[Fe(CN)_6]$), potassium ferrocyanide ($K_4[Fe(CN)_6]$), were obtained from Shanghai Macklin Biochemical Co. Ltd. (Shanghai, China). Phosphate buffer with KCl (PBS, 0.1 M) solutions with pH values 7.4 were prepared with different amounts of NaH_2PO_4 and Na_2HPO_4 and adjusted with 1 M HCl

or 1 M NaOH solutions. Ultrapure deionized water (resistivity: 18.2 MΩ·cm) from a Milli-Q integral water purification system was used throughout the experiments.

2.2. Instrumental

The physicochemical properties of the materials were characterized using the following instruments: X-ray photoelectron spectroscopy (XPS) was performed on an ESCALAB 250Xi instrument (Thermo Fisher, Waltham, MA, USA) with Al Kα radiation. Scanning electron microscopy (SEM) images were acquired using an FEI QUANTA Q400 microscope at an accelerating voltage of 20 kV. Transmission electron microscopy (TEM) images were obtained on an FEI Tecnai G2 F30 microscope operating at 300 kV. Raman spectra were recorded on a DXRxi Raman spectrometer (Thermo Scientific, Waltham, MA, USA) with a 532 nm excitation laser. Static water contact angles were measured at room temperature using a KRUSS DSA25 instrument with pure water droplets. All electrochemical experiments were conducted on an Autolab electrochemical workstation (Metrohm, The Netherlands) using a standard three-electrode system. The system comprised a Cu-LIG or LIG working electrode, an Ag/AgCl reference electrode, and a platinum wire counter electrode. CV measurements were performed at a scan rate of 50 $mV \cdot s^{-1}$. DPV parameters were set as follows: initial potential = −0.2 V, final potential = 0.4 V, step potential = 0.01 V, modulation amplitude = 0.025 V, modulation time = 0.05 s, and interval time = 0.5 s. Electrochemical impedance spectroscopy (EIS) was conducted in a 5 mM $K_3[Fe(CN)_6]/K_4[Fe(CN)_6]$ solution with 0.1 M KCl as the supporting electrolyte; the Nyquist plots were analyzed using NOVA software (version 1.10).

2.2. Preparation of Cu-LIG

The Cu-LIG electrode was fabricated through a sequential laser processing technique. Initially, a square pattern (3 × 0.5 cm^2) was directly scanned onto a polyimide (PI) film using a CO_2 laser under ambient conditions (image density: 1200 PPI; power: 9%; speed: 10%). This one-step laser irradiation converted the irradiated areas into porous LIG. Subsequently, a 20 mM copper-ammonia precursor solution, prepared from copper hydroxide and aqueous ammonia, was uniformly drop-cast onto the LIG working area and air-dried at room temperature. The final step involved a secondary laser scan (9% power, same wavelength as the first step) on the dried precursor-coated LIG.

3. Results and Discussion

3.1. Fabrication and Characterization of Cu-LIG

The Cu-LIG electrode was synthesized *in situ* on a polyimide substrate via a two-step laser process. First, the porous LIG working electrode was directly patterned onto the PI film. Subsequently, a copper-ammonia complex solution was drop-cast onto the LIG and dried. A second laser irradiation was then applied, triggering the rapid photothermal decomposition of the precursor. This instantaneous process broke chemical bonds and released gaseous byproducts (e.g., nitrogen/ammonia), transforming the precursor into Cu NPs, 3D porous foam anchored onto the LIG scaffold.

To assess the microstructural impact of copper doping, the morphologies of pristine and copper-doped LIG were analyzed at multiple scales. SEM images showed that both materials exhibited aligned, parallel grooves at low magnification (Figure 1A,D), resulting from the laser scanning path. Higher-magnification views confirmed that the interconnected 3D porous network was preserved after copper doping (Figure 1B,E), indicating that the essential graphene framework remained intact. However, the Cu-LIG surface appeared notably rougher, with fine, evenly distributed particles suggesting successful surface modification (Figure 1E). For definitive evidence, TEM analysis was performed. While pristine LIG consisted of wrinkled, few-layer graphene sheets with smooth edges (Figure 1C), the Cu-LIG sample exhibited similarly transparent graphene flakes that were densely decorated with uniformly sized spherical nanoparticles (Figure 1F), confirming the incorporation of Cu NPs. The successful incorporation and homogeneous distribution of copper within the graphene matrix were unequivocally verified by energy-dispersive X-ray spectroscopy (EDS). The elemental mapping images (Figure 1G) reveal a uniform spatial distribution of C, N, O, and Cu throughout the Cu-LIG material, directly evidencing the effectiveness of the two-step laser fabrication process.

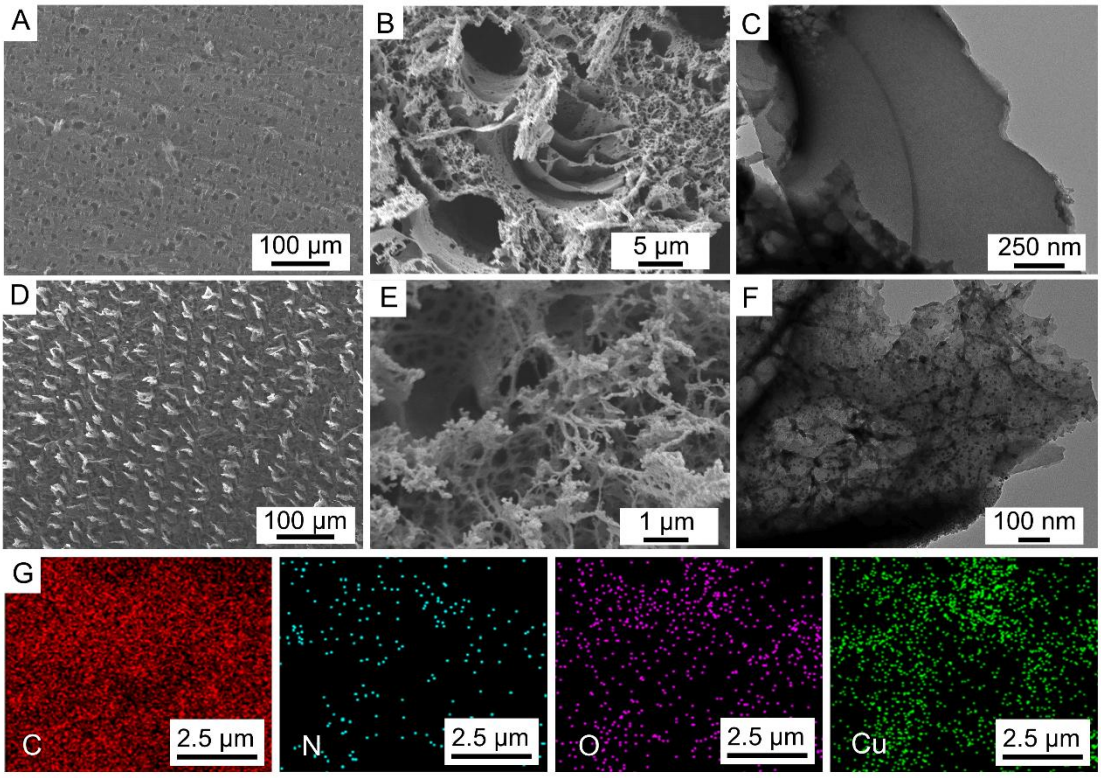

Figure 1. Morphological and structural characterization of LIG and Cu-LIG. (**A**–**C**) SEM and TEM images of pristine LIG at (**A**) low and (**B**) high magnification, and (**C**) a corresponding TEM image. (**D**–**F**) SEM and TEM images of Cu-LIG at (**D**) low and (**E**) high magnification, and (**F**) a corresponding TEM image. (**G**) Elemental mapping images of Cu-LIG, showing the homogeneous distribution of C, N, O, and Cu elements.

To further probe the surface chemistry and chemical states, XPS was employed. The survey spectrum (Figure 2A) clearly confirms the presence of copper in the Cu-LIG composite. High-resolution scans were then used to determine the chemical environment. The Cu 2p spectrum (Figure 2B) exhibited binding energies at 933.4 eV (Cu $2p^{3/2}$) and 953.2 eV (Cu $2p^{1/2}$), with strong satellite features, confirming the dominant presence of Cu(II) [27]. Deconvolution hinted at multiple coordination environments for Cu(II) [26]. Simultaneously, the C 1s spectrum (Figure 2C) detailed the carbon framework, revealing functional groups such as C–O, which are postulated to form C–O–Cu bonds that anchor copper species and enhance electron transfer [28]. This multifaceted analysis reveals that the copper species exist in a complex state with mixed valences and coordinations. This intricate surface chemistry is central to the enhanced electrocatalytic activity, enabling it to efficiently facilitate reactions with diverse biomarkers.

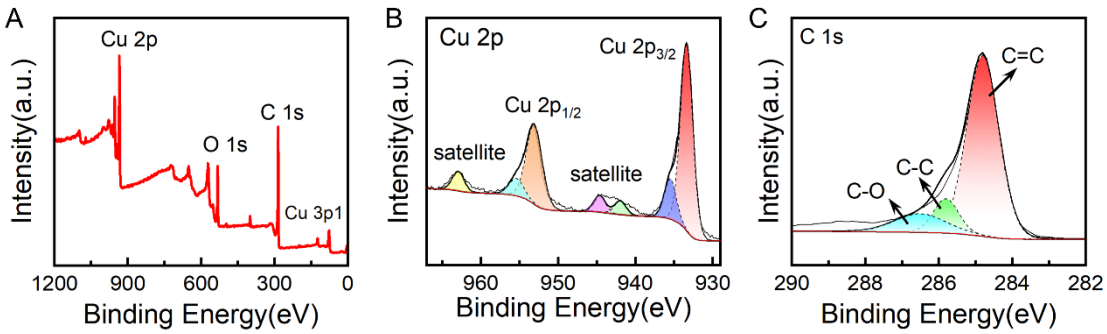

Figure 2. XPS analysis of the Cu-LIG composite. (**A**) XPS survey spectrum. High-resolution spectra of (**B**) Cu 2p and (**C**) C 1s regions.

3.2. Optimization, Electrochemical Performance, and Structural Properties of Cu-LIG Electrodes

A systematic optimization of the Cu-LIG electrode was conducted by evaluating two key parameters: the amount of copper-ammonia precursor and the secondary laser power. First, the influence of copper doped was

investigated. The anodic peak current increased with the amount of precursor, reaching a maximum at 4 μmol (Figure 3A), indicating an optimal density of electroactive sites. Beyond this threshold, the current declined, likely due to excessive coverage leading to pore blockage. Subsequently, the secondary laser power was optimized. A power of 9 W yielded the maximum response (Figure 3B), as lower powers were insufficient for complete precursor reduction, while higher powers risked damaging the delicate 3D graphene network. Consequently, the parameters of 4 μmol precursor and a 9 W laser power were established as optimal for fabrication. The electrochemical performance of the electrode fabricated under these optimal conditions was then evaluated. CV measurements in a $K_3[Fe(CN)_6]/K_4[Fe(CN)_6]$ solution revealed well-defined redox peaks with significantly higher currents compared to the pristine LIG electrode (Figure 3C). This dramatic enhancement is indicative of superior charge transfer kinetics and a larger electroactive area, validating the effectiveness of the optimization process. This optimized protocol was therefore adopted for all subsequent electrode fabrication and testing.

To gain further insights into the interfacial charge transfer properties, EIS was performed over a frequency range of 0.1 Hz to 1 kHz. The corresponding Nyquist plot reveals a substantially smaller semicircular diameter for the Cu-LIG electrode compared to its pristine LIG counterpart, a key observation that confirms the effective reduction of charge-transfer resistance (R_{ct}) and accelerated reaction kinetics attributable to copper doping. Collectively, the CV and EIS results provide congruent evidence that the Cu-LIG composite possesses superior electrocatalytic activity and enhanced conductivity, solidifying its suitability as an excellent platform for sensitive electrochemical detection.

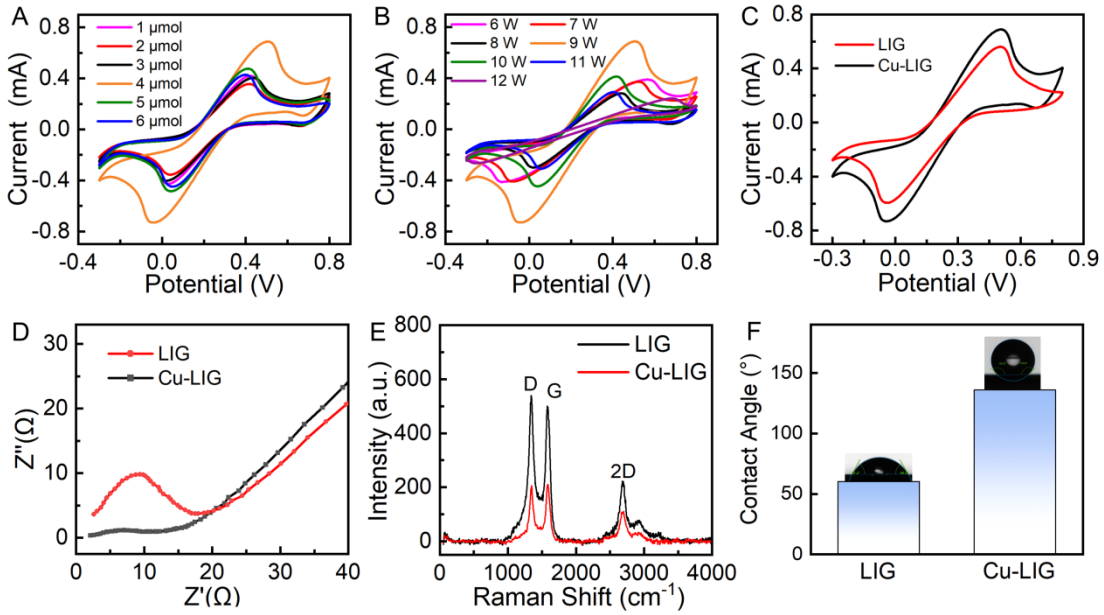

Figure 3. Optimization and multifaceted characterization of the Cu-LIG electrode. (**A**) Optimization of the copper-ammonia precursor amount based on the anodic peak current. (**B**) Optimization of the secondary laser scanning power. (**C**) Comparison of CV curves. (**D**) Corresponding EIS Nyquist plots of Cu-LIG. (**E**) Raman spectra comparison reveals the structural modifications induced by copper doping. (**F**) Static water contact angle measurements show the transition to a hydrophobic surface after copper functionalization.

To comprehensively evaluate the structural and surface property modifications induced by copper doping, Raman spectroscopy and contact angle measurements were employed. First, the Raman spectra of Cu-LIG and pristine LIG were compared. They displayed nearly identical profiles with characteristic D, G, and 2D bands at their expected positions and without significant shifts, demonstrating that the fundamental graphene framework was preserved after the doping process. A detailed analysis of the band intensities revealed subtle yet informative changes: compared to pristine LIG, Cu-LIG exhibited reduced D and G band intensities alongside a slight decrease in the I_D/I_G ratio (from 1.07 to 0.98). This observation is consistent with defect annealing effects induced by the secondary laser treatment [29]. Concurrently, the decrease in the 2D band intensity and the increase in the I_{2D}/I_G ratio (from 0.44 to 0.52) suggest that Cu NPs intercalate between the graphene sheets, thereby effectively suppressing their restacking [23]. Subsequently, the impact on surface wettability was assessed. Static contact angle measurements revealed a dramatic transition: while pristine LIG exhibited hydrophilic behavior with a contact angle of approximately 60°, the Cu-LIG surface became markedly hydrophobic, with a contact angle of 131°. This pronounced shift in wettability strongly suggests a significant alteration in surface chemistry or

topography resulting from the copper incorporation process, which is consistent with the structural changes identified by Raman spectroscopy.

3.3. Analytical Performance for Multiplexed Detection

CV response of the Cu-LIG electrode in a solution containing a mixture of AA, DA, and UA displayed three well-resolved oxidation peaks (Figure 4A–C), demonstrating its exceptional capability for electrochemical discrimination. The peak potential separations were measured to be ΔE(AA-DA) ≈ 0.201 V and ΔE(DA-UA) ≈ 0.111 V (Figure 4D). These substantial differences allow for the clear and simultaneous discrimination of all three biomarkers in a single measurement, a critical advancement for multiplexed sensing.

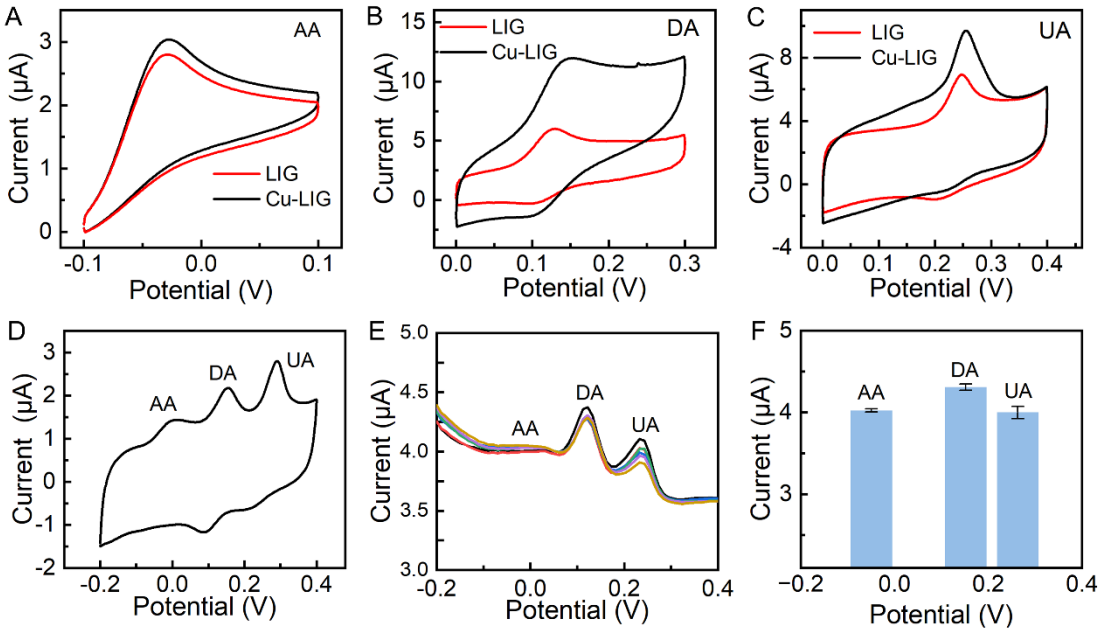

Figure 4. Electrochemical performance of the Cu-LIG electrode for multiplexed sensing. All measurements were performed in 0.1 M PBS (pH 7.4). (**A**–**C**) CV responses of Cu-LIG and pristine LIG electrodes in solutions containing individual analytes: (**A**) 100 μM AA, (**B**) 100 μM DA, and (**C**) 100 μM UA. (**D**) CV of the Cu-LIG electrode in a mixture containing AA, DA, and UA, demonstrating well-resolved oxidation peaks. (**E**) Reproducibility assessment of six independently fabricated sensors. (**F**) Corresponding current versus potential plot for the data in (**E**).

To assess the practical reliability and manufacturing consistency of the Cu-LIG sensor, we measured the response of six electrodes fabricated in separate batches under identical conditions (Figure 4E,F). The minimal variance observed in the signals generated from a solution containing AA (50 μM), DA (100 μM), and UA (100 μM) underscores the exceptional reproducibility of the sensor.

The detection of the Cu-LIG sensor towards each target analyte (AA, DA, UA) was individually calibrated using DPV under optimized conditions in 0.1 M PBS (pH 7.4). The electrolyte and pH were selected to mimic the physiological conditions of sweat and align with standard methodologies in the field, ensuring comparability with established literature. As demonstrated in Figure 5A–C, the DPV responses exhibited three well-defined oxidation peaks at approximately −0.02 V (AA), 0.15 V (DA), and 0.263 V (UA). A marked increase in the peak current was observed for each analyte with increasing its concentration, confirming a strong and specific electrochemical response.

The Cu-LIG electrode was rigorously evaluated for each analyte, demonstrating well-defined linear responses and high sensitivity across the board (Figure 5D–F). Specifically, AA was quantified over a concentration range of 1 to 100 μM, achieving the limit of detection of 0.28 μM (3S/N), which comfortably spans its relevant physiological levels in sweat. DA exhibited a wide linear range from 8 to 100 μM with an LOD of 1.3 μM (3S/N). UA showed the most sensitive response, with an excellent linear range from 1 to 80 μM and the lowest LOD of 0.3 μM (3S/N), making it highly advantageous for the precise monitoring of metabolic disorders such as gout. These collective results unequivocally demonstrate that the Cu-LIG electrode provides high sensitivity and wide linear ranges for all three target analytes, solidifying its reliability for the simultaneous quantification of multiple biomarkers within complex biological samples like sweat.

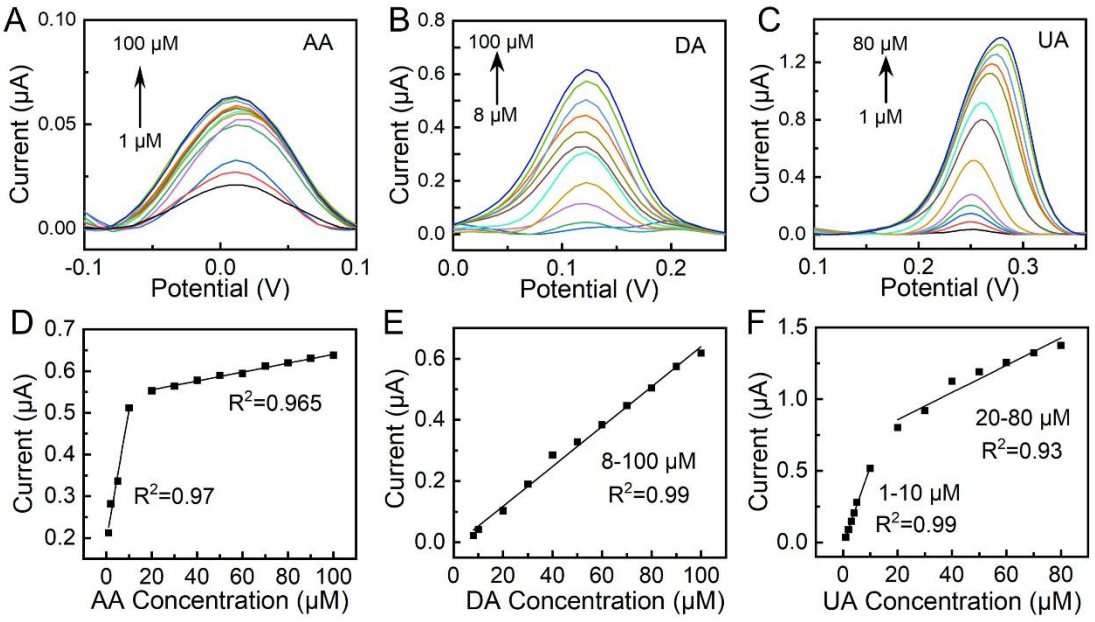

Figure 5. Individual sensing performance and calibration of the Cu-LIG sensor. All DPV measurements were conducted in 0.1 M PBS (pH 7.4). (**A**–**C**) Quantitative DPV responses for progressively increasing concentrations of individual analytes: (**A**) AA, (**B**) DA, and (**C**) UA. (**D**–**F**) The corresponding calibration plots of peak current versus concentration for (**D**) AA, (**E**) DA, and (**F**) UA, which were used to determine the sensitivity and linear detection range for each biomarker.

3.4. Analytical Performance in Complex Matrices

The anti-interference ability and selectivity of the Cu-LIG sensor for multiplexed detection were critically assessed in mixed analyte solutions using DPV under conditions simulating complex samples. To investigate potential cross-interference, experiments were designed where the concentration of one analyte was systematically varied while the concentrations of the other two were maintained constant. The concentration ranges were selected to cover the physiologically relevant levels of each biomarker in human sweat [30], and the specific points chosen for the interference study (Figure 6) were optimized to clearly demonstrate the absence of cross-talk. The resulting DPV responses consistently showed three well-resolved peaks at stable potentials (Figure 6A–C). Most importantly, a linear increase in peak current was exclusively observed for the analyte whose concentration was being varied, while the signals for the other two remained unchanged (Figure 6D–F). This exclusive linear response for each target, without significant cross-talk, unambiguously confirms the sensor's exceptional capability for selective multi-analyte detection in mixtures. A positive shift in the oxidation peak potential is observed for the target analytes as their concentration increases (Figures 5 and 6). This trend aligns with previously reported behavior for copper-based catalysts [31]. The phenomenon is typically explained by an oxidation mechanism at the electrode interface where the copper active sites cycle between different oxidation states (e.g., Cu^{+}/Cu^{2+}). The increasing analyte concentration likely accelerates this redox cycling process, thereby requiring a higher applied potential to drive the oxidation reaction, which manifests as the observed positive peak shift.

To assess the practical selectivity of the Cu-LIG electrode for real-world scenarios, its performance was evaluated against common interferents found in sweat and other physiological fluids. These included inorganic ions (NH_4^+ Ca^{2+}, Cl^-; 1 mM) and small organic molecules (glucose, 100 μM; urea 1 mM; lactate 1 mM), each tested at physiologically relevant concentrations [32,33]. The chosen interference represents common inorganic ions and organic metabolites found in sweat at physiologically significant levels [30]. Remarkably, as shown in Figure 7, the introduction of these potential interferents resulted in negligible variation in the oxidation peak currents for AA, DA, and UA, with no appreciable shift in their respective peak potentials. This exceptional resistance to interference underscores the electrode's robust selectivity, which is a critical attribute for reliable sensing in complex biological matrices like sweat.

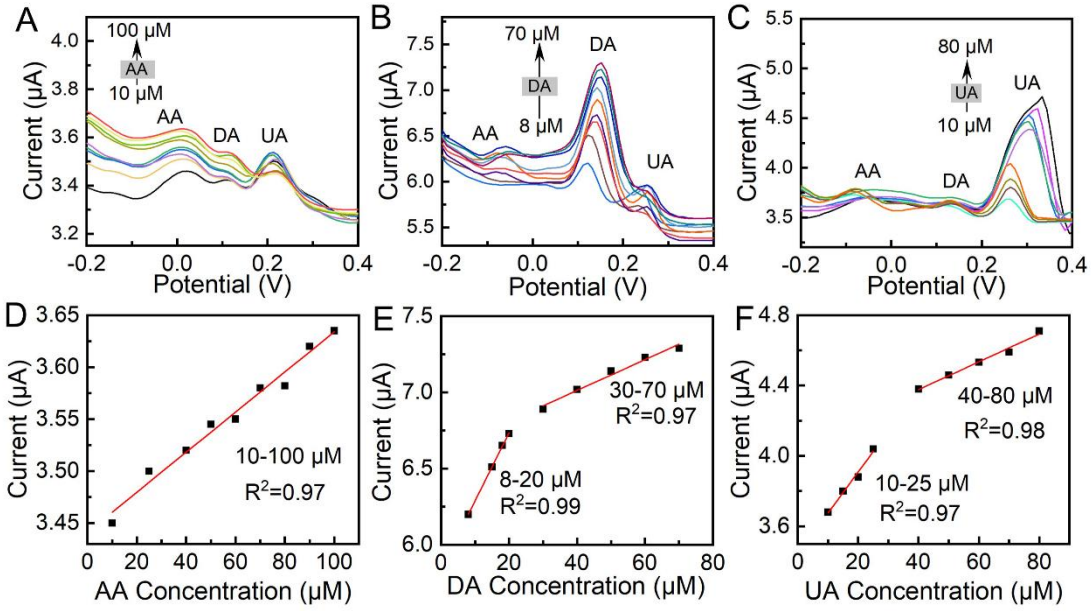

Figure 6. Investigation of selective multiplexed detection with the Cu-LIG sensor. (**A**–**C**) DPV responses obtained in 0.1 M PBS (pH 7.4) for varying concentrations of one analyte against a fixed background of the other two, demonstrating the selective response for (**A**) AA (10–100 μM) with 5 μM DA and 10 μM UA, (**B**) DA (8–70 μM) with 10 μM AA and 10 μM UA, and (**C**) UA (10–80 μM) with 10 μM AA and 5 μM DA. (**D**–**F**) The corresponding calibration curves of peak current versus concentration for (**D**) AA, (**E**) DA, and (**F**) UA, confirming minimal cross-interference and a linear response specific to each target analyte.

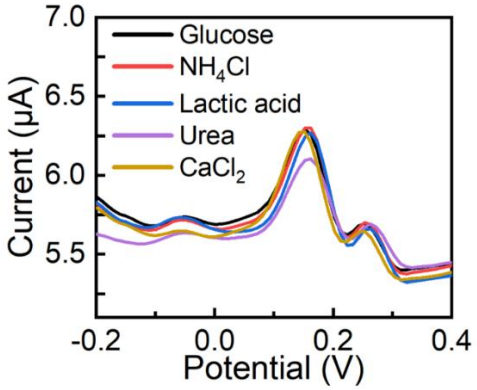

Figure 7. Anti-interference performance of the Cu-LIG sensor. DPV responses demonstrating the minimal impact of common physiological interferents on the detection of AA, DA, and UA.

To validate the sensor's performance under simulated real-world conditions, a standard addition method was conducted in an artificial sweat matrix (0.1 wt% lactic acid and 0.1 wt% urea in PBS, pH 7.4). Different concentrations of the target analytes, spanning their respective physiological ranges in human sweat, were spiked into the matrix. The recovery rates for all analytes were consistently between 95% and 105%, unequivocally confirming the high accuracy and practical applicability of the Cu-LIG sensor for the analysis of complex real-world samples (Table 1).

Table 1. Determination of AA, DA and UA in artificial human sweat ($n = 3$).

Biomarkers	Standard Added (μM)	Total Found (μM)	Recovery (%)	RSD (%)
AA	20	19.1	95.5%	4.8%
DA	8	8.2	102.7%	2.9%
UA	10	9.7	97.8%	3.4%

4. Conclusions

In summary, we developed a synergistic strategy that integrates laser induction with *in situ* metal doping to fabricate a versatile, flexible electrochemical interface. This approach utilizes precise secondary laser modulation to achieve concurrent functionalization of the graphene substrate and the one-step construction of mixed-valence copper (Cu^{2+}/Cu^{+}) active centers, effectively overcoming the traditional trade-off between sensitivity and selectivity in multiplexed biosensing. The resulting Cu-LIG electrode demonstrates remarkable electrocatalytic activity and specific recognition capabilities. Its superior analytical performance for the simultaneous detection of three key biomarkers was rigorously validated in complex physiological matrices. This study thereby offers not only a robust sensing platform for wearable personalized health monitoring, but also establishes a foundational methodology for designing high-performance, multiplexed bioelectronic devices through precision interface engineering. Future work will focus on integrating the electrode into a fully functional wearable system and further optimizing its mechanical flexibility to ensure reliable operation and user comfort under dynamic, real-world conditions. These developments are essential for translating laboratory-based sensing into practical, on-body health monitoring applications.

Author Contributions

H.C., H.Z., M.G., N.C. and X.L.: experimental operation, data analysis, and writing (original draft preparation); X.C.: references arrangement; P.G. and C.G.: project design, writing (reviewing and editing). All authors have read and agreed to the published version of the manuscript.

Funding

We gratefully appreciate the financial support from the Open Research Fund of Observation and Research Station of Seawater Intrusion and Soil Salinization, Laizhou Bay, Ministry of Natural Resources (2025LZORS008), Research Foundation for Distinguished Scholars of Qingdao Agricultural University (665-1122005), and Shandong Provincial Natural Science Foundation (ZR2023QB003).

Data Availability Statement

All data are available in the article. Additional requests can be directed to the corresponding author.

Conflicts of Interest

The authors declare no conflict of interest.

Use of AI and AI-Assisted Technologies

No AI tools were utilized for this paper.

References

1. Shin, J.; Song, J.W.; Flavin, M.T.; et al. A non-contact wearable device for monitoring epidermal molecular flux. *Nature* **2025**, *640*, 375–383. https://doi.org/10.1038/s41586-025-08825-2.
2. Xu, C.; Song, Y.; Sempionatto, J.R.; et al. A physicochemical-sensing electronic skin for stress response monitoring. *Nat. Electron.* **2024**, *7*, 168–179.
3. Kim, S.-R.; Zhan, Y.; Davis, N.; et al. Electrodermal activity as a proxy for sweat rate monitoring during physical and mental activities. *Nat. Electron.* **2025**, *8*, 353–361.
4. Yang, Y.; Song, Y.; Bo, X.; et al. A laser-engraved wearable sensor for sensitive detection of uric acid and tyrosine in sweat. *Nat. Biotechnol.* **2020**, *38*, 217–224.
5. Wang, M.; Ye, C.; Yang, Y.; et al. Printable molecule-selective core–shell nanoparticles for wearable and implantable sensing. *Nat. Mater.* **2025**, *24*, 589–598.
6. Zhong, B.; Qin, X.; Xu, H.; et al. Interindividual- and blood-correlated sweat phenylalanine multimodal analytical biochips for tracking exercise metabolism. *Nat. Commun.* **2024**, *15*, 624. https://doi.org/10.1038/s41467-024-44751-z.
7. Ma, S.; Wan, Z.A.; Wang, C.; et al. Ultra-Sensitive and Stable Multiplexed Biosensors Array in Fully Printed and Integrated Platforms for Reliable Perspiration Analysis. *Adv. Mater.* **2024**, *36*, 2311106. https://doi.org/10.1002/adma.202311106.
8. Huang, W.; Xu, Y.; Yang, Y.; et al. Wearable Sensor for Continuous Monitoring Multiple Biofluids: Improved Performances by Conductive Metal-Organic Framework with Dual-Redox Sites on Flexible Graphene Fiber

Microelectrode. *Adv. Funct. Mater.* **2025**, *35*, 2424018. https://doi.org/10.1002/adfm.202424018.
9. Hao, Z.; Fang, X.; Wang, Z.; et al. Intelligent Wearable Graphene Nano-Electronics with Switchable Surface Wettability Capabilities for Autonomous Sweat Enrichment-Purification-Analysis. *Adv. Funct. Mater.* **2024**, *34*, 2400947. https://doi.org/10.1002/adfm.202400947.
10. Mi, Z.; Xia, Y.; Dong, H.; et al. Microfluidic Wearable Electrochemical Sensor Based on MOF-Derived Hexagonal Rod-Shaped Porous Carbon for Sweat Metabolite and Electrolyte Analysis. *Anal. Chem.* **2024**, *96*, 16676–16685. https://doi.org/10.1021/acs.analchem.4c02950.
11. Davis, N.; Heikenfeld, J.; Milla, C.; et al. The challenges and promise of sweat sensing. *Nat. Biotechnol.* **2024**, *42*, 860–871. https://doi.org/10.1038/s41587-023-02059-1.
12. Wang, M.; Yang, Y.; Min, J.; et al. A wearable electrochemical biosensor for the monitoring of metabolites and nutrients. *Nat. Biomed. Eng.* **2022**, *6*, 1225–1235. https://doi.org/10.1038/s41551-022-00916-z.
13. Tu, J.; Min, J.; Song, Y.; et al. A wireless patch for the monitoring of C-reactive protein in sweat. *Nat. Biomed. Eng.* **2023**, *7*, 1293–1306. https://doi.org/10.1038/s41551-023-01059-5.
14. Xu, T.-Q.; Zhang, Q.-L.; Zheng, J.-N.; et al. Simultaneous determination of dopamine and uric acid in the presence of ascorbic acid using Pt nanoparticles supported on reduced graphene oxide. *Electrochim. Acta* **2014**, *115*, 109–115. https://doi.org/10.1016/j.electacta.2013.10.147.
15. Zheng, X.; Zhou, X.; Ji, X.; et al. Simultaneous determination of ascorbic acid, dopamine and uric acid using poly(4-aminobutyric acid) modified glassy carbon electrode. *Sens. Actuators B Chem.* **2013**, *178*, 359–365. https://doi.org/10.1016/j.snb.2012.12.115.
16. Mwaurah, M.M.; Mathiyarasu, J.; Vinu Mohan, A.M. MWCNTs-Beta-Cyclodextrin-reduced graphene oxide gel based electrochemical sensor for simultaneous detection of dopamine and uric acid in human sweat samples. *Carbohydr. Polym.* **2025**, *350*, 123060. https://doi.org/10.1016/j.carbpol.2024.123060.
17. Bhole, V.; Choi, J.W.J.; Woo Kim, S.; et al. Serum Uric Acid Levels and the Risk of Type 2 Diabetes: A Prospective Study. *Am. J. Med.* **2010**, *123*, 957–961. https://doi.org/10.1016/j.amjmed.2010.03.027.
18. Feig, D.I.; Kang, D.-H.; Johnson, R.J. Uric Acid and Cardiovascular Risk. *N. Engl. J. Med.* **2008**, *359*, 1811–1821. https://doi.org/10.1056/NEJMra0800885.
19. Kohagura, K.; Kochi, M.; Miyagi, T.; et al. An association between uric acid levels and renal arteriolopathy in chronic kidney disease: A biopsy-based study. *Hypertens. Res.* **2013**, *36*, 43–49. https://doi.org/10.1038/hr.2012.135.
20. Major, T.J.; Dalbeth, N.; Stahl, E.A.; et al. An update on the genetics of hyperuricaemia and gout. *Nat. Rev. Rheumatol.* **2018**, *14*, 341–353. https://doi.org/10.1038/s41584-018-0004-x.
21. Choudhury, S.; Zafar, S.; Deepak, D.; et al. A surface modified laser-induced graphene based flexible biosensor for multiplexed sweat analysis. *J. Mater. Chem. B* **2025**, *13*, 274–287. https://doi.org/10.1039/D4TB01936A.
22. Xu, G.; Jarjes, Z.A.; Wang, H.-W.; et al. Detection of Neurotransmitters by Three-Dimensional Laser-Scribed Graphene Grass Electrodes. *ACS Appl. Mater. Interfaces* **2018**, *10*, 42136–42145. https://doi.org/10.1021/acsami.8b16692.
23. Feng, Z.; Geng, Z.; Pan, S.; et al. *In situ* patterning of nickel/sulfur-codoped laser-induced graphene electrode for selective electrocatalytic valorization of glycerol. *Appl. Catal. B Environ. Energy* **2024**, *353*, 124101. https://doi.org/10.1016/j.apcatb.2024.124101.
24. Qing, Z.; Bai, A.; Xing, S.; et al. Progress in biosensor based on DNA-templated copper nanoparticles. *Biosens. Bioelectron.* **2019**, *137*, 96–109. https://doi.org/10.1016/j.bios.2019.05.014.
25. Singh, A.; Hazarika, A.; Dutta, L.; et al. A fully handwritten-on-paper copper nanoparticle ink-based electroanalytical sweat glucose biosensor fabricated using dual-step pencil and pen approach. *Anal. Chim. Acta* **2022**, *1227*, 340257. https://doi.org/10.1016/j.aca.2022.340257.
26. Zhang, Y.; Li, N.; Xiang, Y.; et al. A flexible non-enzymatic glucose sensor based on copper nanoparticles anchored on laser-induced graphene. *Carbon* **2020**, *156*, 506–513. https://doi.org/10.1016/j.carbon.2019.10.006.
27. Jia, B.; Zhao, Y.; Zhang, Z.; et al. Borax promotes the facile formation of hollow structure in Cu single crystalline nanoparticles for multifunctional electrocatalysis. *Inorg. Chem. Front.* **2019**, *6*, 893–902. https://doi.org/10.1039/C8QI01330F.
28. Liu, X.; Xiang, J.; Xue, Y.; et al. Plant wearable sensor based on flexible laser-induced Fe-doped graphene for *in situ* monitoring salicylic acid under salt stress. *Sens. Actuators B* **2025**, *440*, 137931. https://doi.org/10.1016/j.snb.2025.137931.
29. Nguyen, V.T.; Le, H.D.; Nguyen, V.C.; et al. Synthesis of multi-layer graphene films on copper tape by atmospheric pressure chemical vapor deposition method. *Adv. Nat. Sci. Nanosci. Nanotechnol.* **2013**, *4*, 035012. https://doi.org/10.1088/2043-6262/4/3/035012.
30. Bariya, M.; Nyein, H.Y.Y.; Javey, A. Wearable sweat sensors. *Nat. Electron.* **2018**, *1*, 160–171. https://doi.org/10.1038/s41928-018-0043-y.
31. Ibarlucea, B.; Pérez Roig, A.; Belyaev, D.; et al. Electrochemical detection of ascorbic acid in artificial sweat using a

flexible alginate/CuO-modified electrode. *Microchim. Acta* **2020**, *187*, 520.
32. Yu, R.; Deng, Z.; Sharel, P.E.; et al. Highly specific and sensitive quantification of uric acid in sweat using a dual boron-doped diamond electrode. *Sens. Actuators B* **2025**, *426*, 137031. https://doi.org/10.1016/j.snb.2024.137031.
33. Midander, K.; Julander, A.; Kettelarij, J.; et al. Testing in artificial sweat—Is less more? Comparison of metal release in two different artificial sweat solutions. *Regul. Toxicol. Pharm.* **2016**, *81*, 381–386. https://doi.org/10.1016/j.yrtph.2016.09.021.